

PAPER

Dynamic 3D measurement of thermal deformation based on geometric-constrained stereo-matching with a stereo microscopic system

To cite this article: Yan Hu *et al* 2019 *Meas. Sci. Technol.* **30** 125007

View the [article online](#) for updates and enhancements.

Dynamic 3D measurement of thermal deformation based on geometric-constrained stereo-matching with a stereo microscopic system

Yan Hu^{1,2}, Yichao Liang^{1,2}, Tianyang Tao^{1,2}, Shijie Feng^{1,2}, Chao Zuo^{1,2}, Yuzhen Zhang¹ and Qian Chen¹

¹ Jiangsu Key Laboratory of Spectral Imaging & Intelligent Sense, Nanjing University of Science and Technology, Nanjing, Jiangsu Province 210094, People's Republic of China

² Smart Computational Imaging (SCI) Laboratory, Nanjing University of Science and Technology, Nanjing, Jiangsu Province 210094, People's Republic of China

E-mail: zuochao@njust.edu.cn

Received 13 April 2019, revised 6 July 2019

Accepted for publication 25 July 2019

Published 17 September 2019



CrossMark

Abstract

In three-dimensional (3D) shape measurement applications based on absolute phase matching in fringe projection profilometry, measurement accuracy can be improved by using denser fringes under the pre-condition that the phase ambiguities can be successfully removed after phase unwrapping. In real-time measurement situations, the number of fringe patterns is limited to reduce motion-induced errors, which does, however, pose more difficulties for the absolute phase recovery of dense fringes. In this paper, we propose a stereo phase matching method that takes advantage of the high accuracy of denser fringes and the high efficiency of using only two different fringe frequencies. The phase map is divided into several sub-areas, and in each sub-area the phase is unwrapped independently. The stereo-matched pixel is selected from the distributed candidates in these sub-areas by geometric constraints. Experimental results show that only five patterns are needed to perform a high-accuracy real-time 3D measurement of the thermally induced deformation of the sample under different heating temperatures based on a telecentric stereo microscopic system.

Keywords: three-dimensional sensing, optical metrology, binocular and stereopsis, phase unwrapping

 Supplementary material for this article is available [online](#)

(Some figures may appear in colour only in the online journal)

1. Introduction

With recent developments in digital projection, imaging and processing hardware, optical three-dimensional (3D) surface measurement techniques have evolved rapidly. In particular, real-time 3D measurements have been widely applied in but not limited to mechanical engineering, industrial monitoring, computer vision, virtual reality, biomedicine and other industrial applications, owing to the availability of low-cost,

fast, noncontact, high-resolution structured light projection systems [1–3]. Since real-time 3D measurement techniques using fringe projection have been proposed, many techniques, including color-encoded projection techniques [4, 5], gray-scale indexing [6–8], Fourier-transform profilometry [9–12], sequential projection techniques [13, 14] and hybrid methods [15–17], have found their way into practical applications.

In a typical fringe projection 3D measurement application, we calculate the phase values from the fringe images captured

by the camera and obtain the matching relationship between multi-views based on phase matching algorithms [18–24]. In real-time measurement applications, we need to use as few fringe patterns as possible to reduce motion-induced measurement errors [3, 25–27]. However, the correctness of the phase unwrapping will not be guaranteed when the fringe density is increased significantly. The fringe density can be increased by using Fourier fringe profilometry [2, 28], but for isolated objects and the discontinuity surface, a temporal phase unwrapping process is still required [12]. To use a higher fringe density without adding the image number or using denser fringes based on fewer fringe images, scholars have proposed geometric-constraint-based methods to assist phase matching between different views [29, 30]. However, in these methods, one frequency fringe image is still unable to help further increase the fringe density. To accurately unwrap the phase of the fringe images with higher frequency, researchers have proposed embedding speckles or specially designed codewords into the fringe patterns in phase unwrapping free applications [29, 31]. However, the measurement speed is limited because of the complex correlation algorithm. Dual frequency absolute phase retrieval methods are also widely used in fast 3D measurements [27, 32–36]. The commonly used phase unwrapping technique projects a coarse unit frequency image and uses the calculated phase to help unwrap the more accurate phase maps [27, 37]. However, the frequency still cannot be too high because the noise will cause phase order deviations. Dual frequency methods based on reference plane [32] and geometric constraints [38] have been proposed to retrieve the absolute phase from fringe images with a higher frequency. The phase of the fringe with a relatively lower frequency is unwrapped first based on some spatial information. To reconstruct the absolute 3D data, the calibration of the projector is unavoidable, and involves a back projection calculation process, increasing the calibration complexity.

To take advantage of the geometric constraint technique for dual frequency phase unwrapping and avoid the complicated procedure of projector calibration, we propose a phase matching method that divides the phase map of the fringes into four sub-areas. In each sub-area, the phase is unwrapped using the hierarchical temporal phase unwrapping approach [39] to ensure the high accuracy of the retrieved phase value. In order to determine the correct matching point from the candidates in different phase sub-areas, the geometric constraint and left-right consistency check techniques are used. Once the matching point is obtained, the accuracy of the resultant disparity is enhanced to sub-pixel level by using inverse linear interpolation [40]. The main advantage of the proposed method is that we can achieve higher measurement precision by using the same number of fringe patterns as the traditional method, but without involving projector calibration. The effectiveness of the proposed method is verified by real-time 3D measurement of the thermally induced shape deformation based on a microscopic telecentric stereo vision system, achieving a non-ambiguous 3D measurement speed of 20 frames per second.

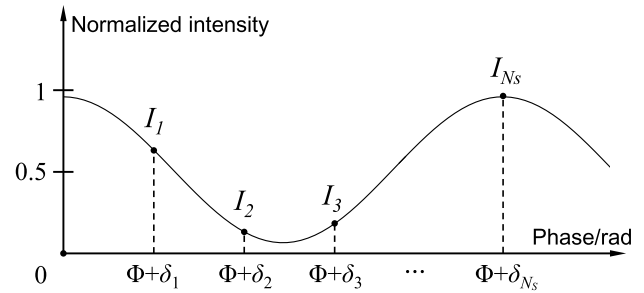


Figure 1. Sketch map of the relation between the intensity and the shifted phase in a phase shifting process.

2. Methods for phase retrieval

2.1. Phase shifting algorithm

With recent developments in the area of digital display, digital projectors have been increasingly applied as projection units in active 3D measurement systems. Based on the amount of controllable phase shifting, the projected intensity with δ_n phase shifting can be easily accomplished. Correspondingly, the recorded fringe image with δ_n phase shifting can be expressed by

$$I_n(u, v) = I_0(u, v) \{1 + \alpha(u, v) \cos[\Phi(u, v) + \delta_n]\}, \quad (1)$$

where (u, v) is the pixel coordinate of the camera, I_0 is the average intensity, α is the fringe contrast, Φ is the phase distribution to be measured, and δ_n is the shifted reference phase ($n = 1, \dots, N$).

The intensities in equation (1) are as shown in figure 1. The phase step δ_n is strictly controlled, so that the phase distribution can be calculated independently over no less than three phase-shifted intensities, based on minimizing a criterion concerning the difference between the ideal intensities and the captured intensities [41]. In particular, if δ_n is equally divided by an integer N_S into the range of $[0, 2\pi)$, we can apply the standard N_S -step phase shifting algorithm [42] to calculate the phase. However, due to the periodicity of sinusoidal waveforms, we can only obtain the wrapped phase ϕ corresponding to Φ as [43]

$$\phi = -\arctan \left[\frac{\sum_{n=1}^{N_S} I_n \sin(\delta_n)}{\sum_{n=1}^{N_S} I_n \cos(\delta_n)} \right]. \quad (2)$$

2.2. Phase unwrapping

The common idea of phase unwrapping algorithms is to unwrap the phase with the aid of one additional wrapped phase map with different fringe periods: λ_l and λ_h . Suppose the two wrapped phases ϕ_l and ϕ_h corresponding to the respective continuous phase maps Φ_l and Φ_h are both retrieved from the phase shifting algorithm using equation (2) or other phase detection approaches [44, 45], the relation between (Φ_l, Φ_h) and (ϕ_l, ϕ_h) can be written as

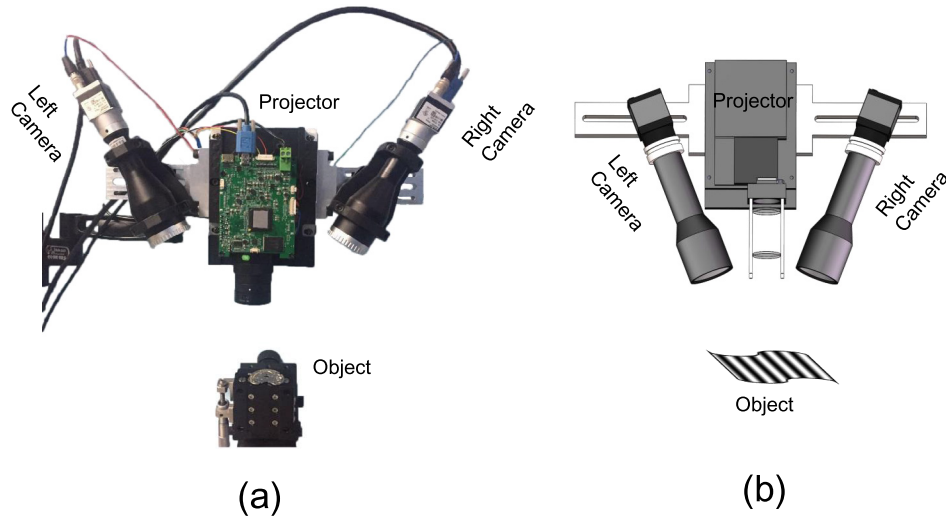


Figure 2. (a) Experimental system; (b) simplified structure model of the system.

$$\begin{cases} \Phi_l = \phi_l + 2\pi k_l \\ \Phi_h = \phi_h + 2\pi k_h \end{cases}, \quad (3)$$

where k_h and k_l are the respective integer fringe orders. It has been proven that among the commonly used phase unwrapping algorithms, hierarchical algorithms can achieve the best phase measurement accuracy (sensitivity) since they can achieve the largest unambiguous measurement range [39]. In the hierarchical algorithm, there is no phase unwrapping required for ϕ_l , that is $\Phi_l = \phi_l$. The fringe order k_h for the higher frequency fringe can be obtained easily as [37]

$$k_h = \text{Round} \left[\frac{(\lambda_l/\lambda_h) \phi_l - \phi_h}{2\pi} \right]. \quad (4)$$

It is proved that the ‘2 + 1’ step phase shifting algorithm has the best frequency-to-frame ratio [46], which means we only need to use five fringe images in total to acquire the ‘unwrapped’ phase map. The fringe images with higher frequency are made up of three standard phase shifting patterns— I_{h1} , I_{h2} and I_{h3} —from which the phase retrieved is ϕ_h . The fringe patterns with a lower frequency are made up of two fringe images, which are the first two images from the standard three-step phase shifting patterns, I_{l1} and I_{l2} . The third fringe image I_{l3} can be obtained by [47]

$$I_{l3} = I_{h1} + I_{h2} + I_{h3} - I_{l1} - I_{l2}. \quad (5)$$

Then both ϕ_l and ϕ_h are calculated using equation (2) and thus the absolute phase map Φ_h can be acquired from equations (3) and (4). When the final absolute phase is scaled into the same range $[0, 2\pi)$, the phase error variance can be stated as [39].

$$\sigma_\Phi^2 = \frac{2\sigma^2}{N_S f^2 B^2}. \quad (6)$$

Here, σ is the variance of a Gaussian distributed additive noise. N_S is the phase shifting step number, f is the fringe frequency, indicating the fringe density, and B is the fringe modulation. Since the phase shifts are confirmed, to acquire a higher phase accuracy, we should use patterns with a higher frequency (f). However, when the fringe frequency is too large, the phase

unwrapping will become unstable because of the inherent noise of other types of error source in the recovered wrapped phase, which limits the success rate of phase unwrapping. So it is necessary to study methods that can unwrap the phase map of denser fringes with limited fringe patterns.

3. Phase stereo-matching based on geometric constraint

A 3D reconstruction is realized based on a well-calibrated multi-view fringe projection setup. In a dual-view setup, as shown in figure 2, the task is to find the matching pixel pairs of the two cameras and then reconstruct the 3D data based on the calibrated parameters of the system which is composed of two telecentric cameras and a digital projector. A point \mathbf{P} in the world coordinates system is imaged on the point \mathbf{p} based on the telecentric camera imaging model as [40]

$$\begin{bmatrix} \mathbf{p} \\ 1 \end{bmatrix} = \mathbf{A} \begin{bmatrix} \mathbf{R}_{2 \times 3} & \mathbf{t}_{2 \times 1} \\ \mathbf{0}_{1 \times 3} & 1 \end{bmatrix} \begin{bmatrix} \mathbf{P} \\ 1 \end{bmatrix} = \mathbf{H} \begin{bmatrix} \mathbf{P} \\ 1 \end{bmatrix}, \quad (7)$$

where \mathbf{R} is the rotation matrix and \mathbf{t} is the translation vector. \mathbf{H} is the homography matrix, which transforms the world coordinates of objects into their corresponding image coordinate. \mathbf{A} is the intrinsic matrix of the telecentric camera with m being the effective magnification of the lens and (u_0, v_0) the image coordinate of the optical center:

$$\mathbf{A} = \begin{bmatrix} m & 0 & u_0 \\ 0 & m & v_0 \\ 0 & 0 & 1 \end{bmatrix}. \quad (8)$$

The method used to calibrate the system refers to our proposed method [40]. If a possible matched pixel pair is determined, we can obtain four equations based on the two camera imaging models, as stated by equation (7). By solving the equations, \mathbf{P} , which contains the 3D data can be calculated. In order to check the correctness of the pixel pair, we can see if the reconstructed depth or the lateral position is in

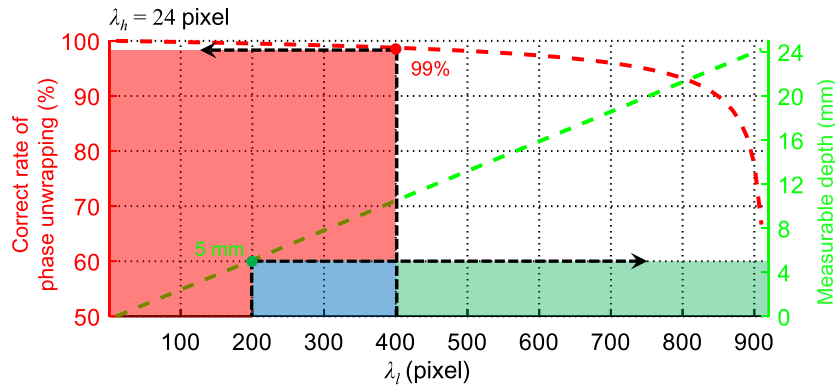


Figure 3. Variation of the measurable depth and correct rate of phase unwrapping as λ_l increases when $\lambda_h = 24$ pixels.

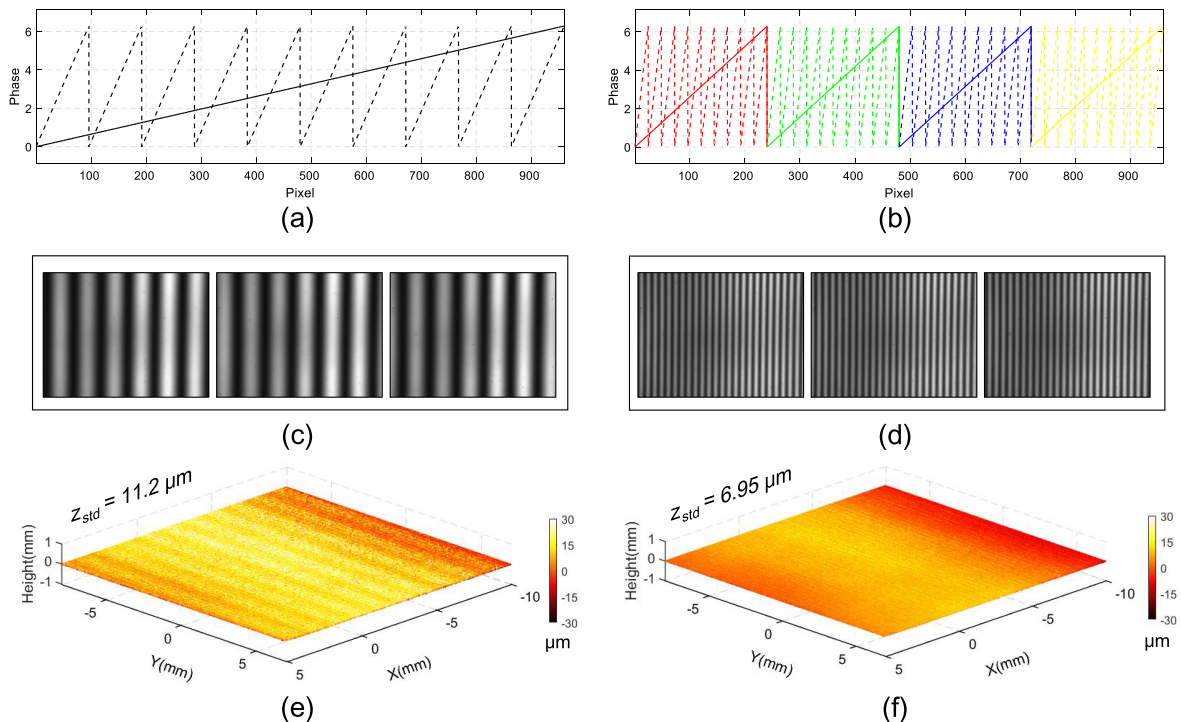


Figure 4. The comparison result using the traditional method and our proposed method. (a) The wrapped phase distribution with $\lambda_h = 96$; (b) the wrapped phase distribution with $\lambda_h = 24$; (c) and (d) the captured three phase shifting fringe images with $\lambda_h = 96$ and $\lambda_h = 24$, respectively; (e) and (f) reconstructed 3D data of the ceramic plane with $\lambda_h = 96$ and $\lambda_h = 24$, respectively.

a reasonable measurement volume. To obtain high-accuracy matched pixel pairs, we try to use the retrieved phase from dense fringes to help realize the sub-pixel stereo-matching of the two telecentric cameras.

Since the fringe frequency cannot be very high when only using two of them in a hierarchical algorithm, we propose a method that divides the phase space into multiple sub-areas so that it can be at least several times larger. To legitimately design the size of the sub-area, we need to consider specific parameters of the system, like the depth of view, fringe pattern resolution, fringe contrast, system arrangement, etc. Studies have shown that the measurement error is proportional to the square of the fringe period [39], so the first step is to find the optimum fringe frequency f_{opt} of the system by continuously changing λ_h and check the value of σ_{Φ}^2 in equation (6) [46]. To determine λ_l , we need to consider two aspects. As shown

in figure 3, we simulate a situation in which the measurable depth and the correct rate of phase unwrapping are the two variables examined. Assume λ_h is a constant variable that equals 24 pixels. Gaussian white noise is added to the fringe images, and the system structure uses the calibrated parameters of our setup, as shown in figure 2.

On the one hand, to obtain an acceptable correct rate of phase unwrapping that is larger than 99%, λ_l should be smaller than a threshold, which corresponds to the red region in figure 3. On the other hand, the smaller λ_l is, the more sub-areas there will be. When more sub-areas divide the phase space, there will be more stereo-matching candidates, which limits the measurable depth range. The threshold of the measurable depth here is set as 5 mm, and that is to say λ_l should also be larger than the threshold, which corresponds to the green region in figure 3. Therefore, there will be an

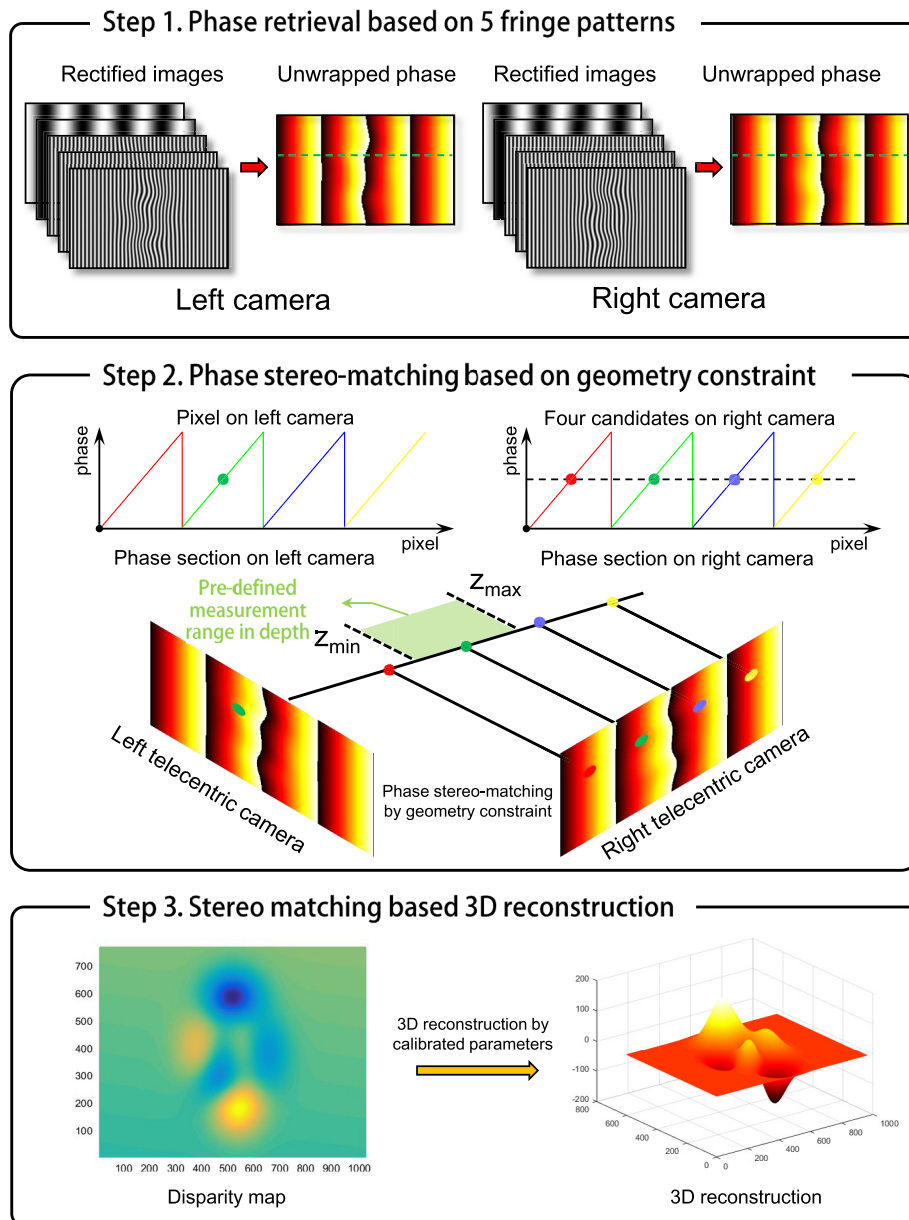


Figure 5. The flowchart of the proposed dynamic 3D measurement method.

overlapping blue region in which λ_l satisfies both conditions, as shown in figure 3.

In our system, the resolution of the projector in the horizontal direction is 912 and the optimum fringe period λ_h is found as 24 pixels. λ_l is determined as 240 pixels, and thus λ_l/λ_h is exactly the integer 10. If for a particular system there is no overlapping blue region in figure 3, then we can lower the optimal frequency (f_{opt}). In this way, the phase unwrapping success rate can be improved because λ_l/λ_h is smaller, and then the red region in figure 3 will be larger. The red and green areas will however overlap and λ_l can be selected to finally obtain a complete measurement. Figure 4 shows a comparison result using a traditional method and our proposed method to measure a ceramic plane. By using the traditional hierarchical phase unwrapping method with $\lambda_l = 912$ and $\lambda_h = 96$, the ultimate fringe number is less than 10, as shown in figure 4(a).

By dividing the phase space into four sub-areas, as shown in figure 4(b), the ultimate phase space will be four times larger. In each sub-area (covered using different colors in figure 4(b)), the phase is unwrapped by the hierarchical temporal phase unwrapping algorithm. The measured 3D results from both methods are as shown in figures 4(e) and (f). As we can see, by enlarging the fringe frequency, the error distribution is much smaller than that in figure 4(e). The corresponding standard deviations of the measured data in figures 4(e) and (f) are $11.2 \mu\text{m}$ and $6.95 \mu\text{m}$, respectively.

Compared with our previously proposed method [38], which conducts a geometric constraint with the phase calculated from fringe images with a lower frequency, the method proposed in this paper first unwraps the phase in each sub-area and conducts a geometric constraint with the phase calculated from fringe images with a higher frequency. As we

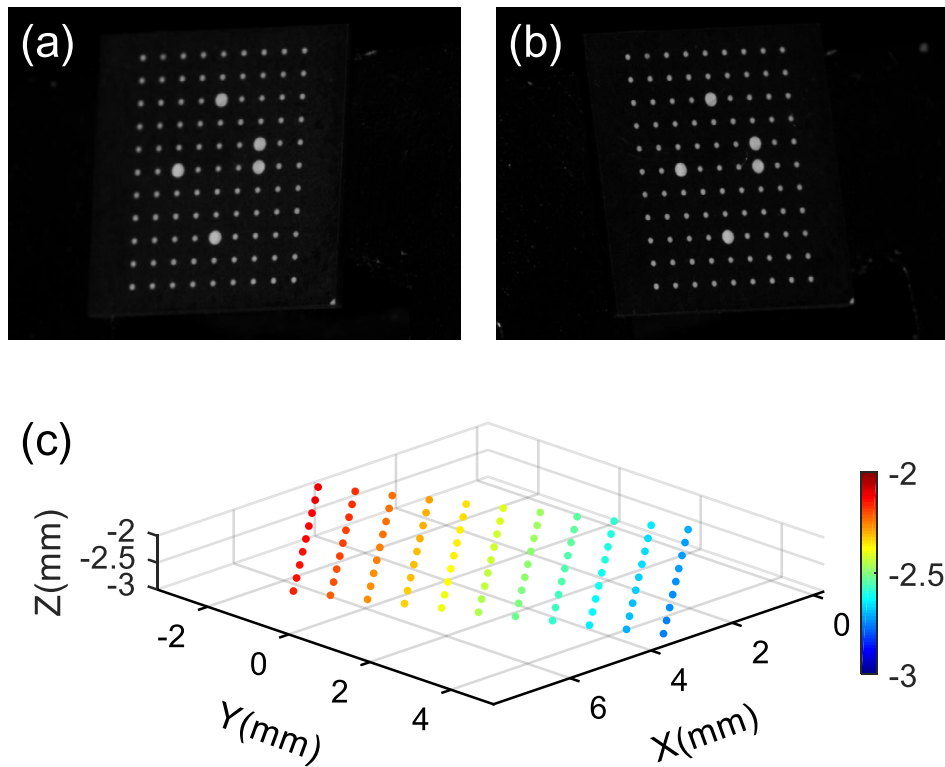


Figure 6. A 3D reconstruction of the centers of the markers on the calibration board: (a) and (b) the rectified image pair of the calibration board; (c) the 3D distribution of the reconstructed centres of the markers with the depth color-coded.

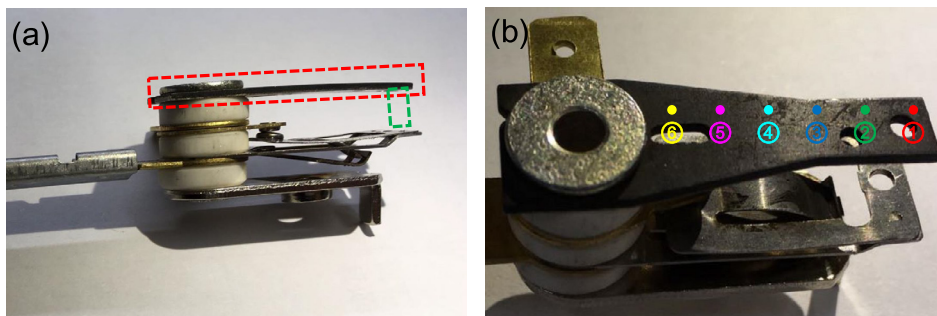


Figure 7. The measured sample. (a) The red rectangular mark is the tested surface which bends when heated. The pressure conducting component, which is supposed to be at the green rectangular mark is taken away; (b) the six measured positions marked with different colors.

know, a higher frequency fringe gives a better phase accuracy, and thus the geometric constraint should be used after phase unwrapping. Another difference between these two methods is that the calibration of our method does not involve projector calibration, so a left-right consistency check process is applied to increase the accuracy of the phase stereo-matching.

To make the proposed method more understandable, we provide a flowchart containing the whole process of the method, as shown in figure 5. Step 1 is the phase calculation from using five fringe patterns, from which two ‘unwrapped’ phase maps corresponding to the left and right camera respectively are obtained. Step 2 is the stereo-matching process; for every primary pixel on the left camera, there will be four theoretical candidates on the right camera whose phase values are close to the phase value on the primary pixel. The measurement

range of each pixel on the left camera has been pre-defined so that the correct matched point can be selected with the help of geometric constraints. Once the phase matching from the left camera to the right camera is finished, the same phase matching process from the right camera to the left camera is also performed to ensure the left-right consistency. After the stereo-matching process, we can obtain the disparity map between two telecentric cameras. Step 3 is to reconstruct the 3D point cloud data based on the calibrated parameters of the dual-view system.

It should be noted that in the intersection of two neighboring sub-areas, the phase jump from 2π to 0 (π to $-\pi$) will affect the phase matching. When dealing with the phase candidate searching near the phase jumping areas, the correct phase matched point may be on the other side of the intersection due

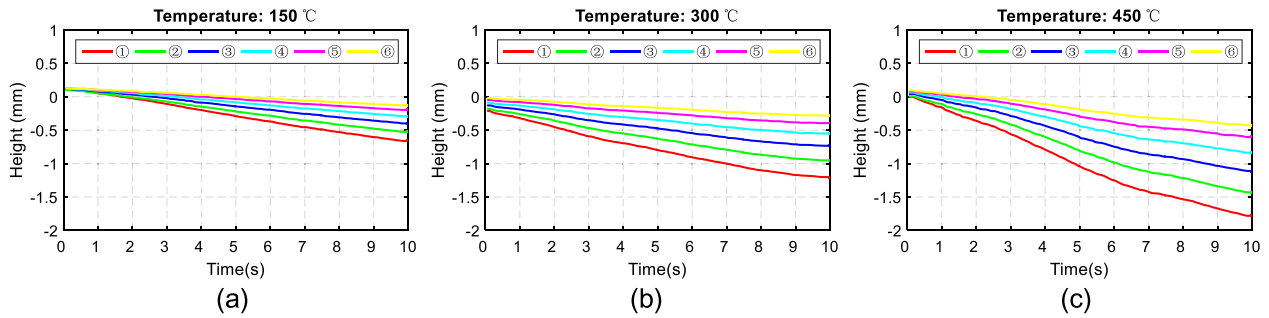


Figure 8. (a)–(c) The depth information of the six marked points in figure 7(b) against time at 150 °C, 300 °C and 450 °C, respectively.

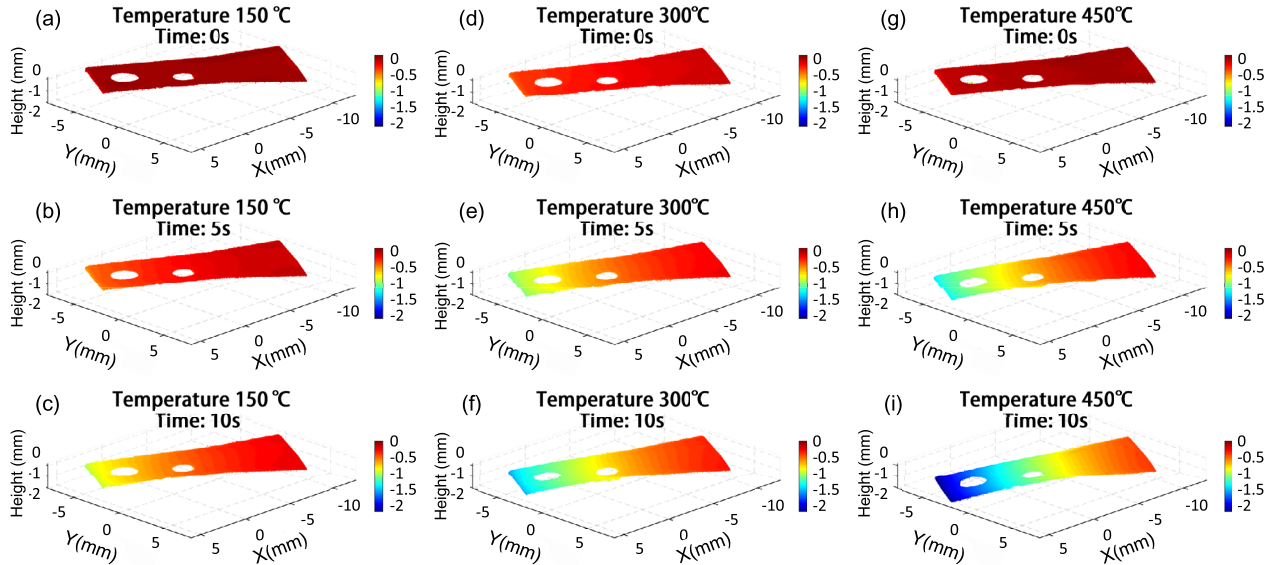


Figure 9. The dynamic absolute 3D measurement of the thermally induced deformation. (a)–(c) The 3D point cloud of the sample at 0 s, 5 s and 10 s, respectively, when heated by 150 °C; (d)–(f) the 3D point cloud of the sample at 0 s, 5 s and 10 s, respectively, when heated by 300 °C; (g)–(i) the 3D point cloud of the sample at 0 s, 5 s and 10 s, respectively, when heated by 450 °C.

to the noise perturbation. So the jumped phase amount (2π) needs to be compensated for the phase matching, and if the phase-compensated point has a closer matched phase value, the matching point should be replaced by the compensated one.

4. Experiment and discussion

To test the performance of the proposed method, we conducted two experiments. The first experiment is a static 3D measurement of the calibration board as shown in figure 6. The absolute 3D position of the centers of the markers on the calibration board is measured to verify the reconstruction accuracy. Figures 6(a) and (b) are the rectified image pair of the averaged intensity of the target. The pixel coordinates of the centres can be extracted and their absolute 3D distributions are reconstructed as presented in figure 6(c), with their depths being color-coded. The distance between two neighboring centers is calculated by $d = \|(x_1, y_1, z_1) - (x_2, y_2, z_2)\|^2$, where d is the distance between two points: (x_1, y_1, z_1) and (x_2, y_2, z_2) in space. There are 90 pairs of neighboring centers in the X direction and 88 pairs in the Y direction. The calculated distances

between the reconstructed centers have a mathematical expectation of 0.6497 mm and an RMSE of 0.0010 mm, which is pretty close to the standard data (0.65 mm, 0.0015 mm) of the calibration board.

To quantitatively measure the thermally induced deformation of a heat sensing material, we used the proposed method to obtain dynamic 3D information of the sample under different heating temperatures. The sample is as shown in figure 7(a). When heated to a certain temperature, the red rectangular mark in figure 7(a) bends its body downwards and generates a force in its normal direction at the far end of the surface. Based on this deformation, a metal contact is connected or disconnected according to the amount of bending, and thus the electric circuit can be controlled depending on the temperature changes.

In our experiments, the temperature is controlled by a heat air gun which can provide an accurate heating temperature from 100 °C to 500 °C. We set the temperature at three different levels, 150 °C, 300 °C, and 450 °C, respectively. The height changes of the six points shown in figure 7(b) under three different temperatures are measured. The recording speed of the camera is 100 frames per second, and in total 10 seconds of data is recorded for each temperature. Figure 8

shows the measured depth information of the six points against time. It is color-coded for the six different points, and the depth changing curves have the same color, as used in both figure 7(b) and figure 8. When the temperature is 150 °C, the metal contact is not active, even though the sample has bent a little bit. When we provide a higher temperature of 300 °C, the metal contact is still inactive since the temperature threshold of the device is 440 °C. However, the bending amount is larger than that when the temperature is 150 °C. The metal contact becomes active at last when we set the temperature to 450 °C. From figure 8(c), we can see that the bending amount is quite a lot larger than that under the other two conditions. Because the recording time of the three measurements is not strictly aligned, the time starting points of figures 8(a)–(c) are not exactly the same.

In order to observe the deformation more clearly, we conducted the dynamic absolute 3D measurement of the sample. Part of the measured results is shown in figure 9. Figures 9(a)–(c) are the 3D point cloud of the sample at 0 s, 5 s and 10 s, respectively, when the sample is heated by 150 °C. Figures 9(d)–(f) are the 3D point cloud of the sample at 0 s, 5 s and 10 s, respectively, when heated by 300 °C. Figures 9(g)–(i) are the 3D point clouds of the sample at 0 s, 5 s and 10 s, respectively, when heated by 450 °C. The dynamic deformation process of the sample under different temperatures can be found in the supplementary media (visualization 1) (stacks.iop.org/MST/30/125007/mmedia).

5. Conclusion

In this paper, we proposed a stereo phase matching method that takes advantage of the high accuracy of denser fringes and the high efficiency of using only two different fringe frequencies based on an easily calibrated microscopic telecentric stereo vision system. By dividing the phase space into several sub-areas, the computational complexity for the localization of the matching candidates using a geometric constraint can be significantly reduced. The fringe density can be much higher than that in traditional methods based on hierarchical temporal phase unwrapping, and higher measurement precision can be achieved by using the same number of fringe patterns as the traditional method without involving the projector calibration.

The experimental results show that our proposed method can measure thermally induced shape deformation with high speed and high accuracy based on a microscopic telecentric stereo vision system, achieving a nonambiguous 3D shape measurement speed of 20 frames per second.

Acknowledgments

This research was funded by the National Key R&D Program of China (2017YFF0106403), the National Natural Science Fund of China (61722506, 61705105, 111574152), the Final Assembly ‘13th Five-Year Plan’ Advanced Research Project of China (30102070102), the Equipment Advanced

Research Fund of China (61404150202), the Key Research and Development Program of Jiangsu Province, China (BE2017162), the Outstanding Youth Foundation of Jiangsu Province of China (BK20170034), the National Defense Science and Technology Foundation of China (0106173), the Six Talent Peaks Project of Jiangsu Province, China (2015-DZXX-009), the 333 Engineering Research Project of Jiangsu Province, China (BRA2016407), the Fundamental Research Funds for the Central Universities (30917011204, 30916011322), the Open Research Fund of the Jiangsu Key Laboratory of Spectral Imaging & Intelligent Sense (3091801410403, 3091601410414), the China Postdoctoral Science Foundation (2017M621747) and the Jiangsu Planned Projects for Postdoctoral Research Funds (1701038A).

ORCID iDs

Yan Hu  <https://orcid.org/0000-0003-1558-1541>

Shijie Feng  <https://orcid.org/0000-0001-8261-5276>

Chao Zuo  <https://orcid.org/0000-0002-1461-0032>

References

- [1] Zhang S and Huang P 2004 High-resolution, real-time 3D shape acquisition *2004 Conference on Computer Vision and Pattern Recognition Workshop (Washington, DC, USA, 27 June–2 July 2004)* (Piscataway, NJ: IEEE) p 28
- [2] Zhang Q and Su X 2005 High-speed optical measurement for the drumhead vibration *Opt. Express* **13** 3110–6
- [3] Zhang S 2010 Recent progresses on real-time 3D shape measurement using digital fringe projection techniques *Opt. Lasers Eng.* **48** 149–58
- [4] Geng Z J 1996 Rainbow three-dimensional camera: new concept of high-speed three-dimensional vision systems *Opt. Eng.* **35** 376–84
- [5] Liu W, Wang Z, Mu G and Fang Z 2000 Color-coded projection grating method for shape measurement with a single exposure *Appl. Opt.* **39** 3504–8
- [6] Payeur P and Desjardins D 2009 Structured light stereoscopic imaging with dynamic pseudo-random patterns *Int. Conf. Image Analysis and Recognition* (Berlin: Springer) pp 687–96
- [7] Le Moigne J and Waxman A M 1988 Structured light patterns for robot mobility *IEEE J. Robot. Autom.* **4** 541–8
- [8] Griffin P M, Narasimhan L S and Yee S R 1992 Generation of uniquely encoded light patterns for range data acquisition *Pattern Recognit.* **25** 609–16
- [9] Takeda M and Mutoh K 1983 Fourier transform profilometry for the automatic measurement of 3D object shapes *Appl. Opt.* **22** 3977–82
- [10] Su X and Chen W 2001 Fourier transform profilometry: a review *Opt. Lasers Eng.* **35** 263–84
- [11] Zhong J and Weng J 2004 Spatial carrier-fringe pattern analysis by means of wavelet transform: wavelet transform profilometry *Appl. Opt.* **43** 4993–8
- [12] Zuo C, Tao T, Feng S, Huang L, Asundi A and Chen Q 2018 Micro Fourier transform profilometry (μ ftp): 3D shape measurement at 10000 frames per second *Opt. Lasers Eng.* **102** 70–91
- [13] Posdamer J L and Altschuler M 1982 Surface measurement by space-encoded projected beam systems *Comput. Graph. Image Process.* **18** 1–17

- [14] Hall-Holt O and Rusinkiewicz S 2001 Stripe boundary codes for real-time structured-light range scanning of moving objects *Proc. 8th IEEE Int. Conf. on Computer Vision (Vancouver, BC, Canada, Canada, 7–14 July 2001)* vol 2 (Piscataway, NJ: IEEE) pp 359–66
- [15] Wang Y, Zhang S and Oliver J H 2011 3D shape measurement technique for multiple rapidly moving objects *Opt. Express* **19** 8539–45
- [16] Zhang S 2010 Flexible 3D shape measurement using projector defocusing: extended measurement range *Opt. Lett.* **35** 934–6
- [17] Kim E-H, Hahn J, Kim H and Lee B 2009 Profilometry without phase unwrapping using multi-frequency and four-step phase-shift sinusoidal fringe projection *Opt. Express* **17** 7818–30
- [18] Zhang S and Huang P S 2006 Novel method for structured light system calibration *Opt. Eng.* **45** 083601
- [19] Huang P S, Zhang C and Chiang F-P 2003 High-speed 3D shape measurement based on digital fringe projection *Opt. Eng.* **42** 163–9
- [20] Koninckx T P, Geys I, Jaeggli T and Van Gool L 2004 A graph cut based adaptive structured light approach for real-time range acquisition *Proc. 2nd Int. Symp. on 3D Data Processing, Visualization and Transmission, 2004. 3DPVT 2004 (Thessaloniki, Greece, 9th September 2004)* (Piscataway, NJ: IEEE) pp 413–21
- [21] Buytaert J A and Dirckx J J 2010 Phase-shifting Moiré topography using optical demodulation on liquid crystal matrices *Opt. Lasers Eng.* **48** 172–81
- [22] Pan J, Huang P S, Zhang S and Chiang F-P 2004 Color n-ary gray code for 3D shape measurement *12th Int. Conf. on Experimental Mechanics* vol 29
- [23] Karpinsky N L, Hoke M, Chen V and Zhang S 2014 High-resolution, real-time three-dimensional shape measurement on graphics processing unit *Opt. Eng.* **53** 024105
- [24] Van der Jeught S, Soons J A and Dirckx J J 2015 Real-time microscopic phase-shifting profilometry *Appl. Opt.* **54** 4953–9
- [25] Zuo C, Chen Q, Gu G, Feng S and Feng F 2012 High-speed three-dimensional profilometry for multiple objects with complex shapes *Opt. Express* **20** 19493–510
- [26] Nguyen H, Nguyen D, Wang Z, Kieu H and Le M 2015 Real-time, high-accuracy 3D imaging and shape measurement *Appl. Opt.* **54** A9–17
- [27] Liu K, Wang Y, Lau D L, Hao Q and Hassebrook L G 2010 Dual-frequency pattern scheme for high-speed 3D shape measurement *Opt. Express* **18** 5229–44
- [28] Hu Y, Chen Q, Zhang Y, Feng S, Tao T, Li H, Yin W and Zuo C 2018 Dynamic microscopic 3D shape measurement based on marker-embedded Fourier transform profilometry *Appl. Opt.* **57** 772–80
- [29] Li Z, Zhong K, Li Y F, Zhou X and Shi Y 2013 Multiview phase shifting: a full-resolution and high-speed 3D measurement framework for arbitrary shape dynamic objects *Opt. Lett.* **38** 1389–91
- [30] Tao T, Chen Q, Da J, Feng S, Hu Y and Zuo C 2016 Real-time 3D shape measurement with composite phase-shifting fringes and multi-view system *Opt. Express* **24** 20253–69
- [31] Pan B, Qian K, Xie H and Asundi A 2009 Two-dimensional digital image correlation for in-plane displacement and strain measurement: a review *Meas. Sci. Technol.* **20** 062001
- [32] Xing Y and Quan C 2018 Enhanced reference-plane-based dual-frequency absolute phase retrieval for depth measurement *Meas. Sci. Technol.* **29** 105003
- [33] Lu J, Mo J, Sun H, Chang Z and Zhao X 2016 Simplified absolute phase retrieval of dual-frequency fringe patterns in fringe projection profilometry *Opt. Commun.* **364** 101–9
- [34] Dai M, Yang F, Liu C and He X 2017 A dual-frequency fringe projection three-dimensional shape measurement system using a DLP 3D projector *Opt. Commun.* **382** 294–301
- [35] Ding Y, Xi J, Yu Y, Cheng W, Wang S and Chicharo J F 2012 Frequency selection in absolute phase maps recovery with two frequency projection fringes *Opt. Express* **20** 13238–51
- [36] Hu Y, Chen Q, Feng S, Tao T, Li H and Zuo C 2017 Real-time microscopic 3D shape measurement based on optimized pulse-width-modulation binary fringe projection *Meas. Sci. Technol.* **28** 075010
- [37] Hu Y, Chen Q, Tao T, Li H and Zuo C 2017 Absolute three-dimensional micro surface profile measurement based on a Greenough-type stereomicroscope *Meas. Sci. Technol.* **28** 045004
- [38] Tao T, Chen Q, Feng S, Hu Y, Zhang M and Zuo C 2017 High-precision real-time 3D shape measurement based on a quad-camera system *J. Opt.* **20** 014009
- [39] Zuo C, Huang L, Zhang M, Chen Q and Asundi A 2016 Temporal phase unwrapping algorithms for fringe projection profilometry: a comparative review *Opt. Lasers Eng.* **85** 84–103
- [40] Hu Y, Chen Q, Feng S, Tao T, Asundi A and Zuo C 2019 A new microscopic telecentric stereo vision system-calibration, rectification, and three-dimensional reconstruction *Opt. Lasers Eng.* **113** 14–22
- [41] Lai G and Yatagai T 1991 Generalized phase-shifting interferometry *J. Opt. Soc. Am. A* **8** 822–7
- [42] Zuo C, Feng S, Huang L, Tao T, Yin W and Chen Q 2018 Phase shifting algorithms for fringe projection profilometry: a review *Opt. Lasers Eng.* **109** 23–59
- [43] Hu Y, Chen Q, Liang Y, Feng S, Tao T and Zuo C 2019 Microscopic 3D measurement of shiny surfaces based on a multi-frequency phase-shifting scheme *Opt. Lasers Eng.* **122**
- [44] Takeda M, Ina H and Kobayashi S 1982 Fourier-transform method of fringe-pattern analysis for computer-based topography and interferometry *J. Opt. Soc. Am. A* **72** 156–60
- [45] Kemao Q 2004 Windowed Fourier transform for fringe pattern analysis *Appl. Opt.* **43** 2695–702
- [46] Zhang M, Chen Q, Tao T, Feng S, Hu Y, Li H and Zuo C 2017 Robust and efficient multi-frequency temporal phase unwrapping: optimal fringe frequency and pattern sequence selection *Opt. Express* **25** 20381–400
- [47] Zuo C, Chen Q, Gu G, Feng S, Feng F, Li R and Shen G 2013 High-speed three-dimensional shape measurement for dynamic scenes using bi-frequency tripolar pulse-width-modulation fringe projection *Opt. Lasers Eng.* **51** 953–60